

A Kalman Filter for Amplitude Estimation in High-Speed Dynamic Mode Atomic Force Microscopy

Michael G. Ruppert, *Student Member, IEEE*, Kai S. Karvinen, *Member, IEEE*,
Samuel L. Wiggins, and S. O. Reza Moheimani, *Fellow, IEEE*

Abstract—A fundamental challenge in dynamic mode atomic force microscopy (AFM) is the estimation of the cantilever oscillation amplitude from the deflection signal, which might be distorted by noise and/or high-frequency components. When the cantilever is excited at resonance, its deflection is typically obtained via narrow-band demodulation using a lock-in amplifier (LIA). However, the bandwidth of this measurement technique is ultimately bounded by the low-pass filter, which must be employed after demodulation to attenuate the component at twice the carrier frequency. Furthermore, to measure the amplitude of multiple frequency components, such as higher eigenmodes and/or higher harmonics in multifrequency AFM, multiple LIAs must be employed. In this paper, the authors propose the estimation of amplitude and phase using a linear time-varying Kalman filter that is easily extended to multiple frequencies. Experimental results are obtained using square-modulated sine waves and closed-loop AFM scans, verifying the performance of the proposed Kalman filter.

Index Terms—Amplitude estimation, atomic force microscopy (AFM), field-programmable gate array (FPGA) implementation, high bandwidth, Kalman filter, state estimation.

I. INTRODUCTION

IN ATOMIC force microscopy (AFM) [1], a microcantilever with a sharp tip is coupled to the sample's surface via nonlinear tip-sample forces. Nanometer-resolution images of a wide variety of materials [2] can be obtained by utilizing feedback control; the controller performs disturbance rejection and estimates the sample topography. The ability to study dynamic biological processes is considered one of the major driving forces behind the development of high-speed tapping-mode AFM (TM-AFM) [3], which requires low tip-sample interaction forces, fast positioning stages, and high-speed cantilevers in order to capture the dynamics on

these time scales [4]. In this operational mode, the cantilever is usually excited near its fundamental resonance frequency and the tapping amplitude is kept constant at a predefined setpoint by a controller commanding the nanopositioner in its vertical direction. When the output of the controller is mapped against the horizontal trajectory of the nanopositioner, a 3-D image of the sample's topography is obtained. High-speed AFM setups therefore require every component in the feedback loop to be optimized; a fast cantilever (high resonance frequency and low quality factor), a fast x -, y -, and z -axis nanopositioner, a high-bandwidth z -axis controller, and a high-speed amplitude estimation technique are essential [5]. Common methods of amplitude estimation, such as rms to dc conversion and the lock-in amplifier (LIA), are typically not suitable for high-speed operation and their limitations have led to the development of fast single wave detectors based on the peak-hold method [6], [7], Fourier technique [8], and real-time integration [9], [10].

One common drawback to the use of rms to dc conversion, the peak-hold technique and the real-time integration technique is their inability to produce accurate amplitude estimates in the presence of noise and/or higher harmonic/eigenmode contributions. As a result, these techniques are incompatible with multifrequency AFM methods [11]. The LIA—a narrow-band technique—is more suitable at rejecting unwanted frequency components, but at the expense of the measurement bandwidth. A high-bandwidth LIA was recently proposed and implemented to address this issue, improving upon the measurement bandwidth of the LIA [12]. However, the bandwidth is still ultimately limited by the low-pass filters, which are required to account for mismatches in the phase.

The application of advanced estimation techniques has proved successful in dynamic mode AFM. The mathematical and system viewpoint considering the cantilever and the tip-sample force as separate subsystems in a feedback loop employs methods from harmonic analysis and power balance [13], [14] promoting the idea that an observer can be constructed to estimate the states position and velocity of the cantilever. Moreover, since the observer does not contain an explicit model of the unknown and nonlinear tip-sample force, the error signal will contain information of the disturbance profile during the transient response of the cantilever [15]–[17]. An analog implementation of the observer was proposed for which the signal-to-noise

Manuscript received December 9, 2014; revised March 19, 2015; accepted May 9, 2015. Date of publication June 5, 2015; date of current version December 21, 2015. Manuscript received in final form May 13, 2015. Recommended by Associate Editor I. Petersen.

M. G. Ruppert and S. L. Wiggins are with the School of Electrical Engineering and Computer Science, The University of Newcastle, Callaghan, NSW 2308, Australia (e-mail: michael.ruppert@uon.edu.au; samuel.wiggins@uon.edu.au).

K. S. Karvinen is with the Institute for Dynamic Systems and Control, ETH Zurich, Zurich 8092, Switzerland (e-mail: kaik@ethz.ch).

S. O. Reza Moheimani is with the Department of Mechanical Engineering, University of Texas at Dallas, Dallas, TX, USA (reza.moheimani@utdallas.edu).

Color versions of one or more of the figures in this paper are available online at <http://ieeexplore.ieee.org>.

Digital Object Identifier 10.1109/TCST.2015.2435654

ratio increases with increasing observer gain, whereas the measurement noise increases as well [18].

In addition, it is possible to directly estimate the tip-sample force in TM-AFM by assuming it takes the form of an impulse train [19]. Formulating the estimation problem as a Kalman filter, the tip-sample force is estimated directly; thus, potentially enabling high-bandwidth z -axis control. Assuming zero-mean Gaussian white noise processes, the Kalman filter produces the optimal state estimate, however, even for general noise sources, the Kalman filter still yields the best linear estimator.

In this contribution, the authors propose the use of a linear Kalman filter to estimate the amplitude and phase of the cantilever deflection without a model of the cantilever itself. Unlike the LIA, which is usually employed to recover the cantilever amplitude from a possibly noisy background, the Kalman filter is not limited by the demodulation low-pass filters and can therefore achieve significantly higher measurement bandwidth. Furthermore, the flexible system representation allows for the simultaneous estimation of multiple frequency components, such as higher eigenmodes and/or harmonics, for which usually a number of LIAs must be employed.

The remainder of this paper is organized as follows. Section II contains a review of amplitude estimation techniques used in dynamic mode AFM, highlighting the limitations in their measurement bandwidth and multifrequency capabilities. In Section III, the model of a sinusoidal signal is derived, which forms the basis of the Kalman filter approach proposed in this contribution and Section IV outlines the discrete Kalman filter equations. The experimental results highlighting the square-modulated sine waves and closed-loop AFM scans are presented in Section V.

II. AMPLITUDE ESTIMATION IN ATOMIC FORCE MICROSCOPY

A. RMS to DC Conversion and Mean Absolute Deviation

One of the earliest forms of amplitude estimation is rms to dc conversion. The rms value s_{rms} of a sinusoidal signal $s(t)$ with a period T is proportional to the amplitude of the signal s_{pk} and is defined as

$$s_{\text{rms}} = \sqrt{\frac{1}{T} \int_t^{t+T} s^2(t) dt} = \frac{s_{\text{pk}}}{\sqrt{2}}. \quad (1)$$

In TM-AFM, regulation of the amplitude of oscillation of the excited mode is required for the estimation of the surface topography. However, in the presence of other frequency components, such as higher eigenmode contributions and/or higher harmonics, rms to dc conversion is unable to accurately determine the oscillation amplitude of the excited mode. Methods of true rms to dc conversion include thermal rms to dc conversion; direct computation, where the amplifiers are used to perform the squaring, averaging, and square rooting functionality; and indirect computation that utilizes feedback [20]. A number of analog and digital true rms to dc converters are available commercially.

In TM-AFM, rms to dc conversion was typically performed using a rectifier circuit and a low-pass filter [5]. However, it must be stressed that this is not rms to dc conversion, but mean absolute deviation [20], which calculates the ac average of the waveform $2s_{\text{pk}}/\pi$. For a pure sinusoidal signal, the output is proportional to the oscillation amplitude, but this technique also suffers from the same drawbacks as rms to dc conversion. Inaccurate amplitude estimates are obtained when additional frequency components are present in the displacement signal and high-frequency oscillations must be removed from the low-bandwidth amplitude estimate. As a result, these techniques often require many cycles for convergence, which severely limits the achievable imaging bandwidth in TM-AFM.

B. Peak-Hold Technique

The peak-hold technique [6] was developed specifically for high-speed TM-AFM imaging. It utilizes sample and hold circuitry to hold both the positive and negative peaks for the duration of a cycle. While this technique offers high measurement bandwidth, it is more susceptible to noise as there are only two measurements per cycle. Furthermore, the presence of harmonics will result in erroneous amplitude estimates and complicates the synchronization of the sample and hold circuitry. Nonetheless, this technique was successfully used to obtain video rate imaging of myosin V by employing very small tip-sample forces [21].

C. Lock-In Amplifier

In comparison with the preceding techniques, the LIA is advantageous since it can extract the amplitude of a specific frequency component from a noisy background. The LIA mixes the input signal consisting of a carrier sine wave and a slowly time-varying amplitude signal $S_0(t)$ of the form

$$s(t) = S_0(t) \sin(\omega t + \phi) \quad (2)$$

with in-phase and quadrature sinusoids to obtain

$$\begin{aligned} s_i(t) &= S_0(t) \sin(\omega t + \phi) \sin \omega t \\ &= \underbrace{\frac{1}{2} S_0(t) \cos \phi}_X - \underbrace{\frac{1}{2} S_0(t) \cos(2\omega t + \phi)}_{\text{low-pass filtered}} \end{aligned} \quad (3)$$

and

$$\begin{aligned} s_q(t) &= S_0(t) \sin(\omega t + \phi) \cos \omega t \\ &= \underbrace{\frac{1}{2} S_0(t) \sin(\phi)}_Y + \underbrace{\frac{1}{2} S_0(t) \sin(2\omega t + \phi)}_{\text{low-pass filtered}}. \end{aligned} \quad (4)$$

With suitable low-pass filtering, the undesirable frequency content at 2ω can be rejected and accurate amplitude and phase estimates can be calculated by

$$S_0(t) = 2\sqrt{X^2 + Y^2} \quad (5)$$

$$\phi = \arctan\left(\frac{Y}{X}\right) \quad (6)$$

where X is the in-phase component and Y is the quadrature component. However, since the low-pass filters must separate

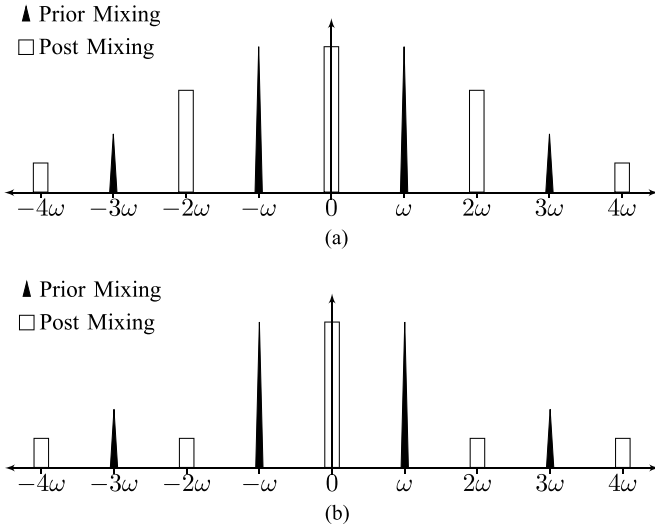


Fig. 1. Comparison of frequency spectra using (a) standard and (b) high-bandwidth LIAs.

the slow time-varying component from the high-frequency oscillations, the measurement bandwidth is limited. This is illustrated in Fig. 1(a) that shows the 2ω component resulting from the mixing process. The low-pass filter bandwidth must be chosen as a compromise between good tracking of $S_0(t)$ and adequate filtering of the high-frequency component.

D. High-Bandwidth Lock-In Amplifier

The high-bandwidth LIA [12] is a novel technique inspired by image rejection mixers [23] and modulated-demodulated control [24]. Here, phase cancellation is employed to exactly cancel the 2ω component for a pure sinusoidal input signal. In practice, a postmixing low-pass filter is still required since circuit mismatches will prevent the exact cancellation. However, since the high-frequency oscillations have been attenuated significantly, the bandwidth of the low-pass filter can be increased, which leads to an increase in measurement bandwidth. Fig. 1(b) highlights the reduction in the high-frequency components situated at 2ω by employing the high-bandwidth LIA technique.

E. Real-Time Integration

The Fourier method is conceptually similar to the LIA, but involves the direct computation of the Fourier series coefficients. While this technique is more robust than the peak-hold technique, it requires accurate timing and integration over an integral number of oscillations [8]. If the Fourier series coefficients are determined digitally, the speed and resolution of the analog-to-digital converter (ADC) will affect the accuracy of the calculation. For microcantilevers with megahertz resonances, such an implementation could be challenging. Another low-latency demodulation method has been proposed based on mixing and postintegration [9], [10] of the in-phase and quadrature components. It was shown that if the integration period is chosen to be an integer multiple of the drive signal period, the integral of the high frequency terms goes to zero. While such precise control over

the integration period is only achievable in digital systems, the implementation of this method is challenging but can be done using finite-impulse response filters. While the simulation results show that low latency can be achieved for a pure sinusoid, in order to reject white noise, multiple oscillation periods must be integrated resulting in a lower measurement bandwidth. The authors are not aware of any published reports on experimental implementations of this method in closed loop.

F. Summary

Table I compares the amplitude estimation techniques discussed so far. It can be observed that while a few specialized methods are able to obtain the amplitude estimates in a single cycle, these methods lack the flexibility to either reject the background noise or to estimate the higher frequency components simultaneously. The high-bandwidth LIA offers a good compromise between the measurement bandwidth and robustness. The following sections will introduce a Kalman filter estimation method that is capable of achieving high-bandwidth estimation of the amplitude and phase and is easily extended to estimate an arbitrary number of higher frequency components.

III. MODELING SINUSOIDAL SIGNALS

A. Time-Invariant Models

1) *Observable Canonical Form*: The homogeneous differential equation describing the motion of a simple harmonic oscillator with resonance frequency ω is given by

$$\ddot{x}(t) + \omega^2 x(t) = 0. \quad (7)$$

This equation can be transformed into the standard phase variable state-space model by choosing the position $x_1 = x(t)$ and the velocity $x_2 = \dot{x}(t)$ as the state variables and position as the output, yielding the following representation:

$$\begin{aligned} \dot{x} &= Ax = \begin{bmatrix} 0 & 1 \\ -\omega^2 & 0 \end{bmatrix} x \\ y &= Cx = [1 \ 0]x. \end{aligned} \quad (8)$$

2) *Modal Canonical Form*: Since A in (8) has two distinct eigenvalues $\lambda_{1,2} = \pm j\omega$, there exists a time-invariant similarity transformation V that maps it into diagonal form. This transformation is given by the set of independent eigenvectors and takes the complex form

$$V = [v_1 \ v_2] = \begin{bmatrix} 1 & j\omega \\ j\omega & \omega^2 \end{bmatrix}. \quad (9)$$

Applying this transformation yields

$$\begin{aligned} \dot{\tilde{x}} &= V^{-1}AV\tilde{x} = \begin{bmatrix} j\omega & 0 \\ 0 & -j\omega \end{bmatrix} \tilde{x} \\ \tilde{y} &= CV\tilde{x} = [1 \ j\omega]\tilde{x}. \end{aligned} \quad (10)$$

Even though the canonical forms (8) and (10) are useful in the analysis and understanding of the state equations, they are generally ill conditioned for numerical computations. This can be observed by calculating the condition number κ that can be

TABLE I
SUMMARY OF AMPLITUDE ESTIMATION METHODS

Method	Amplitude	Phase	Convergence (Cycles)	Robustness to Noise	Reference
Fourier Technique	Yes	Yes	20	Yes	[8]
Lock-In Amplifier	Yes	Yes	6-10	Yes	[22]
RMS to DC	Yes	No	5	No	[20], [6]
High-Bandwidth Lock-In Amplifier	Yes	Yes	2-3	Yes	[12]
Peak Hold	Yes	No	1	No	[6]
Real-Time Integration	Yes	Yes	1	No	[9], [10]

defined with respect to a matrix norm $\|\cdot\|$ of a square matrix M as [25]

$$\kappa(M) = \|M\| \|M^{-1}\|. \quad (11)$$

B. Time-Variant Model

Consider the time-variant transformation

$$T = \begin{bmatrix} \cos(\omega t) & \sin(\omega t) \\ -\omega \sin(\omega t) & \omega \cos(\omega t) \end{bmatrix} \quad (12)$$

and its inverse

$$T^{-1} = \begin{bmatrix} \cos(\omega t) & -\frac{1}{\omega} \sin(\omega t) \\ \sin(\omega t) & \frac{1}{\omega} \cos(\omega t) \end{bmatrix} \quad (13)$$

such that

$$\bar{x} = T^{-1}x. \quad (14)$$

A time-variant state-space representation can be obtained by

$$\begin{aligned} \dot{\bar{x}} &= \frac{d}{dt}(T^{-1}x) \\ &= \frac{d}{dt}(T^{-1})T\bar{x} + T^{-1}AT\bar{x} \\ \bar{y} &= CT\bar{x} \end{aligned} \quad (15)$$

where

$$\frac{d}{dt}(T^{-1}) = \begin{bmatrix} -\omega \sin(\omega t) & -\cos(\omega t) \\ \omega \cos(\omega t) & -\sin(\omega t) \end{bmatrix} \quad (16)$$

and

$$\frac{d}{dt}(T^{-1})T = \begin{bmatrix} 0 & -\omega \\ \omega & 0 \end{bmatrix} \quad (17)$$

$$T^{-1}AT = \begin{bmatrix} 0 & \omega \\ -\omega & 0 \end{bmatrix} \quad (18)$$

which converts (8) into the following form:

$$\begin{aligned} \dot{\bar{x}} &= \begin{bmatrix} 0 & 0 \\ 0 & 0 \end{bmatrix} \bar{x} \\ \bar{y} &= [\cos(\omega t) \quad \sin(\omega t)] \bar{x}. \end{aligned} \quad (19)$$

In other words, since the solution of the standard phase variable model takes the known form of a sinusoid

$$\begin{aligned} x(t) &= A \sin(\omega t + \phi) \\ &= x(0) \cos(\omega t) + \frac{\dot{x}(0)}{\omega} \sin(\omega t) \end{aligned} \quad (20)$$

where the amplitude A and the phase ϕ are determined by the initial conditions, the new state variables and output

can be chosen as random variables such that $\bar{x}_1 = x(0)$, $\bar{x}_2 = (\dot{x}(0)/\omega)$, and $\bar{y} = x(t)$. Note that the output still resembles the position and is represented by the time-varying output vector, but in contrast to (8) the amplitude and phase can be readily recovered via

$$A = \sqrt{\bar{x}_1^2 + \bar{x}_2^2} \quad (21)$$

$$\phi = \arctan\left(\frac{\bar{x}_2}{\bar{x}_1}\right). \quad (22)$$

IV. DISCRETE KALMAN FILTER

A. Single Frequency

The continuous model (19) can be discretized exactly for $t = kT_s$, where T_s is the sampling period, by calculating

$$\begin{aligned} A_k &= e^{AkT_s} = \mathcal{L}^{-1}\{(sI - A)^{-1}\}|_{t=kT_s} \\ &= \mathcal{L}^{-1}\left\{\begin{bmatrix} \frac{1}{s} & 0 \\ 0 & \frac{1}{s} \end{bmatrix}\right\} = I \\ C_k &= C|_{t=kT_s} \end{aligned} \quad (23)$$

which leads to the discrete time-variant model of a single sinusoid

$$\begin{aligned} x_{k+1} &= A_k x_k = \begin{bmatrix} 1 & 0 \\ 0 & 1 \end{bmatrix} \begin{bmatrix} x_1 \\ x_2 \end{bmatrix}_k \\ y_k &= C_k x_k = [\cos(\omega k T_s) \quad \sin(\omega k T_s)] \begin{bmatrix} x_1 \\ x_2 \end{bmatrix}_k \end{aligned} \quad (24)$$

where the states x_{1k} and x_{2k} represent the random variables describing the amplitude and phase. Assuming that the state and output equations are corrupted by zero-mean Gaussian white noise processes w_k and v_k , respectively, the system representation is in the form of the discrete Kalman filter

$$\begin{aligned} x_{k+1} &= A_k x_k + w_k \\ y_k &= C_k x_k + v_k \\ E[w_k w_k^T] &= Q_k \\ E[v_k v_k^T] &= R_k \\ E[w_k v_k^T] &= 0 \end{aligned} \quad (25)$$

where Q_k is the covariance of the process noise and relates to the quality of the model and R_k is the covariance of the measurement noise and relates to the quality of the measurements. The recursive Kalman filter implementation then consists of initializing the estimation with a prior estimate of the state \hat{x} and the covariance matrix P

$$\hat{x}_{0|0} = E[x_0] \quad (26)$$

$$P_{0|0} = E[(x_0 - \hat{x}_{0|0})(x_0 - \hat{x}_{0|0})^T] \quad (27)$$

and then iterating between the prediction step

$$\hat{x}_{k|k-1} = A_k \hat{x}_{k-1|k-1} \quad (28)$$

$$P_{k|k-1} = A_k P_{k-1|k-1} A_k^T + Q_k \quad (29)$$

and the measurement update step by calculating the Kalman gain K_k

$$K_k = P_{k|k-1} C_k^T (C_k P_{k|k-1} C_k^T + R_k)^{-1}. \quad (30)$$

The estimated state must then be corrected

$$\hat{x}_{k|k} = \hat{x}_{k|k-1} + K_k (y_k - C \hat{x}_{k|k-1}) \quad (31)$$

and the covariance matrix can be updated as follows:

$$P_{k|k} = (I - K_k C) P_{k|k-1} (I - K_k C)^T + K_k R_k K_k^T. \quad (32)$$

A similar system description was successfully used in tracking power system voltage phasors [26]. For an in-depth review of the linear Kalman filter, the interested readers are referred to [27] and [28]. Note that (30) has one more equivalent form and (32) has two more equivalent forms [27], which should be chosen to either optimize the speed or the stability of the numerical computations. In this case, (32) was chosen such that the property of symmetry and positive definiteness of the covariance matrix is not lost during computations.

B. Multiple Frequencies and DC Offset

For accurate amplitude estimation in multifrequency AFM, it is necessary to include the higher frequency components, such as higher harmonics and/or eigenmodes in the Kalman filter. This allows for the simultaneous estimation of higher harmonics [29] or higher eigenmodes as is typical in bimodal AFM experiments [30]. Furthermore, the output of the position sensitive detector usually contains a dc offset related to a static deflection of the cantilever or misalignment of the laser and this can lead to systematic errors in the estimate. For a sinusoidal signal containing multiple frequency components and a dc offset of the form

$$\begin{aligned} x(t) &= C + \sum_{i=1}^n A_i \sin(\omega_i t + \phi_i) \\ &= C + \sum_{i=1}^n x_{1,i} \cos(\omega_i t) + x_{2,i} \sin(\omega_i t) \end{aligned} \quad (33)$$

the discrete state-space representation (24) can be extended to yield

$$\begin{aligned} x_{k+1} &= \begin{bmatrix} 1 & 0 & \cdots & 0 & 0 & 0 \\ 0 & 1 & \cdots & 0 & 0 & 0 \\ \vdots & \vdots & \ddots & \vdots & \vdots & \vdots \\ 0 & 0 & \cdots & 1 & 0 & 0 \\ 0 & 0 & \cdots & 0 & 1 & 0 \\ 0 & 0 & \cdots & 0 & 0 & 1 \end{bmatrix} \begin{bmatrix} x_{1,1} \\ x_{2,1} \\ \vdots \\ x_{1,n} \\ x_{2,n} \\ x_{dc} \end{bmatrix}_k \\ y_k &= \begin{bmatrix} \cos(\omega_1 k T_s) \\ \sin(\omega_1 k T_s) \\ \vdots \\ \cos(\omega_n k T_s) \\ \sin(\omega_n k T_s) \\ 1 \end{bmatrix}^T \begin{bmatrix} x_{1,1} \\ x_{2,1} \\ \vdots \\ x_{1,n} \\ x_{2,n} \\ x_{dc} \end{bmatrix}_k \end{aligned} \quad (34)$$

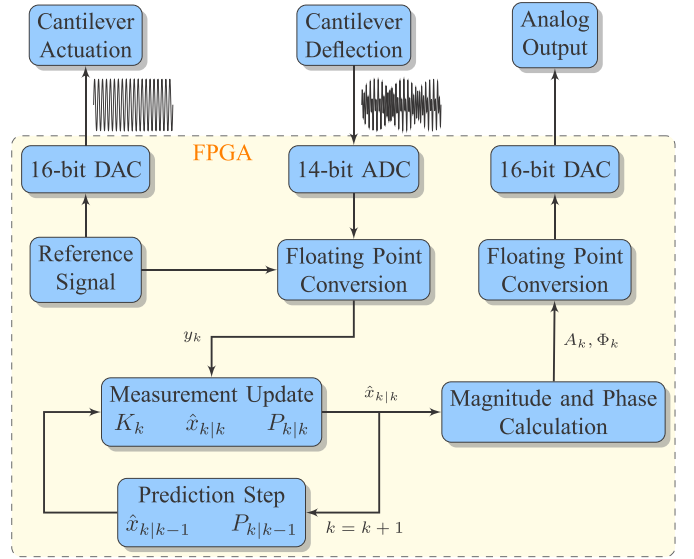


Fig. 2. Block diagram of the main modules implemented on the FPGA and the interface to the cantilever.

which is capable of estimating the amplitude of n frequencies and an unknown dc offset. These frequencies can relate to either the mechanical resonance frequencies of the cantilever or the higher harmonics of the fundamental resonance frequency or both. It should be emphasized that all significant frequencies to be estimated must be known and accounted for; however, this is not a stringent condition as the resonance frequencies and the higher harmonics can be easily determined.

V. EXPERIMENTAL RESULTS

A. Implementation

The discrete Kalman filter was implemented recursively on a Xilinx Kintex7 field-programmable gate array (FPGA) clocked at 245 MHz and interfaced with an FMC150 high-speed dc-coupled input/output (I/O) card. The FMC150 is an external I/O card featuring a dual channel, 14-bit 250 MSa/s ADC, along with a dual-channel 16-bit 800 MSa/s digital-to-analog converter (DAC). These ports maintain a very high sampling rate, which is required for the application of a high-speed Kalman filter. The FMC150 is configured on the Kintex7 with a range of ± 1 V for the ADC and likewise for the DAC to represent the values at $[-1, 1]$ and an output of ± 1 V. A block diagram of the main components implemented on the FPGA and their interface to the cantilever is shown in Fig. 2. The Xilinx block direct digital synthesizer is used to generate the reference sine and cosine signals, which can also be used to drive the cantilever. The Kalman filter loop is closed through the use of registers, each storing a 32-bit floating point value for one period. At each cycle, the measurement update is fed to the prediction step and the state estimates are passed through a magnitude and phase calculation block, which converts the data into a form compatible with the DAC.

B. Square-Modulated Sine Waves

To validate the filter performance, a test bench was set up consisting of external function generators to produce

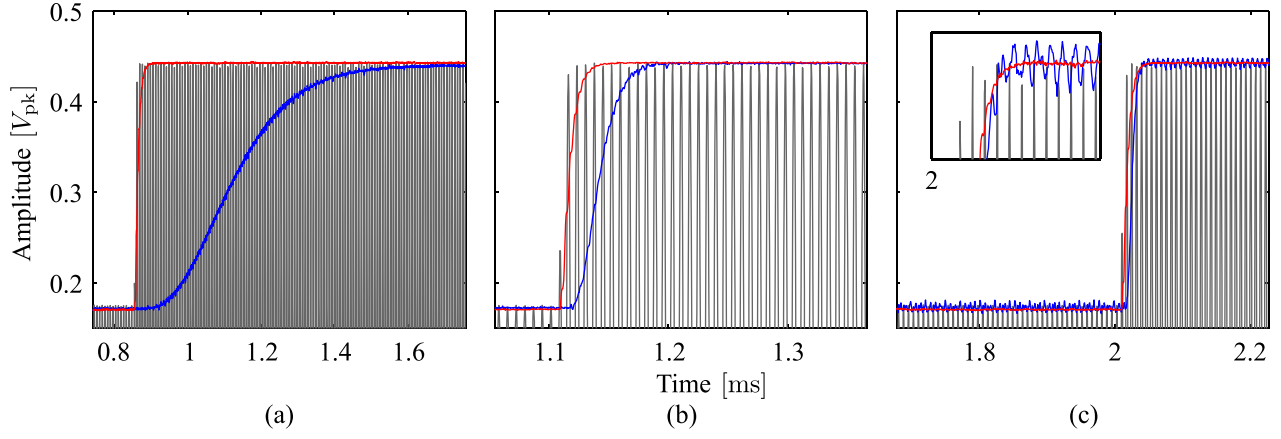


Fig. 3. Carrier sine wave with $f_c = 137$ kHz amplitude modulated by a square wave with $f_m = 500$ Hz (—), amplitude estimate from Kalman filter (—) and demodulated amplitude signal with LIA (—) having a low-pass cutoff frequency of (a) $f = 1$ kHz, (b) $f = 10$ kHz, and (c) $f = 30$ kHz.

square amplitude modulated sine waves and a Zürich Instruments HF2LI LIA was employed to provide the benchmark amplitude estimate. The carrier frequency was chosen to be $f_c = 137$ kHz, which resembles the typical fundamental resonance frequency of noncontact cantilevers, such as the NT-MDT NSG01. The modulation frequency was chosen to be $f_m = 500$ Hz, which resembles a very high scan speed in TM-AFM. In Fig. 3, it can be observed that the Kalman filter is able to produce a high-bandwidth amplitude estimate while rejecting signal noise. However, the bandwidth of the postmixing low-pass filter of the LIA has to be increased to at least 30 kHz in order to obtain a similar high-bandwidth amplitude estimate. Noticeable oscillations can be observed in Fig. 3(c) since the $2\omega_c$ component cannot be adequately filtered.

C. Dynamic Mode Atomic Force Microscopy

To compare the quality of the amplitude estimates during TM-AFM operation, an experiment utilizing a Nanosurf Easyscan2 AFM was set up to simulate a tip-sample disturbance from regularly spaced rectangular sample features. A schematic of this setup is shown in Fig. 4(a). A budget sensor TAP190 cantilever with a resonance frequency of 189 kHz was used; the quality factor was set to 141 using Q -control [31] (not shown) resulting in an approximate bandwidth of 4.2 kHz. To maintain the cantilever's oscillation amplitude at a setpoint of 50% of its free-air amplitude and to compensate for the sample's simulated topography $D(t)$, the z -axis controller commands the z -axis actuator, in this case, a custom-built high-bandwidth piezoelectric nanopositioner with a resonance frequency of 65 kHz [32], [33]. The z -axis proportional integral (PI) controller has been tuned to achieve minimum rise time with no overshoot for each experiment. The disturbance rejection performance of the closed loop can be assessed by the speed at which the disturbance profile is tracked and additional noise introduced. Fig. 5(a)–(c) highlights that the tracking performance can be improved substantially with higher filter bandwidths when using the LIA in order to increase the overall closed-loop bandwidth. However, as shown in Fig. 5(c), when the cutoff frequency is too high, the filter is unable to significantly attenuate the 2ω component.

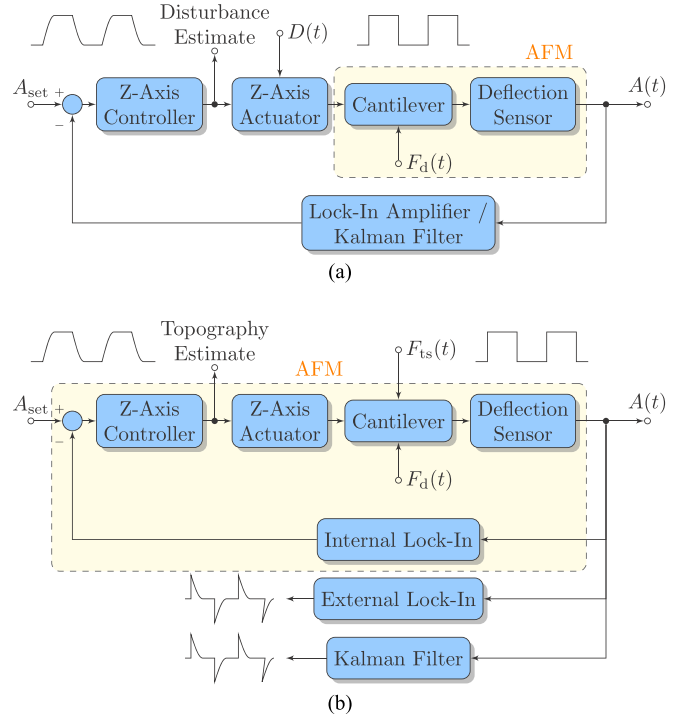


Fig. 4. Block diagram of the AFM operating in tapping-mode (a) with external disturbance modulation $D(t)$ and (b) parallel external LIA and Kalman filter. $F_d(t)$ is the excitation force acting on the base of the cantilever and $F_{ts}(t)$ is the tip-sample force acting on the tip of the cantilever.

The Kalman filter is advantageous, since it offers high-bandwidth amplitude estimation and therefore the smallest tracking error without the unwanted high-frequency components, which can be observed in Fig. 5(d). The minimal offset and drift, which can be observed is due to hysteresis and creep in the z -axis actuator.

Furthermore, experiments were conducted with the LIA and Kalman filter set up adjacent to the AFM control loop, as shown in Fig. 4(b). An NT-MDT NTEGRA AFM was used for these experiments, which houses a built-in xyz piezoelectric tube scanner and z -axis PI controller. An NT-MDT TGZ3 calibration grating with periodic rectangular features of height $h = 520 \pm 3$ nm was scanned at $20 \mu\text{m/s}$. Fig. 6 shows

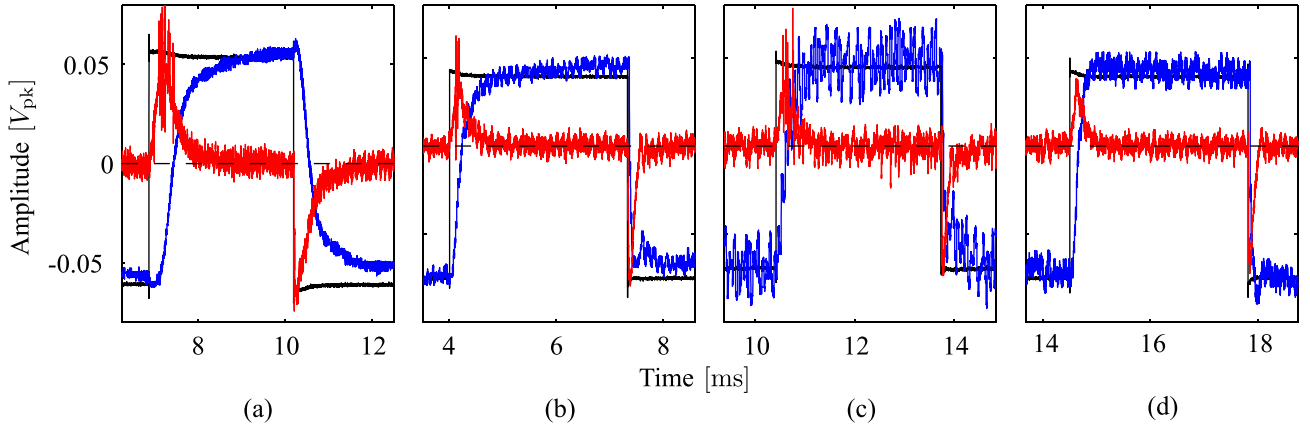


Fig. 5. Cantilever input disturbance with $f_m = 150$ Hz (—), error signal (—), and z -axis controller output (—) representing the disturbance estimate based on the demodulated amplitude signal with LIA having a low-pass cutoff frequency of (a) $f = 1$ kHz, (b) $f = 30$ kHz, and (c) $f = 80$ kHz and using the (d) Kalman filter for amplitude estimation.

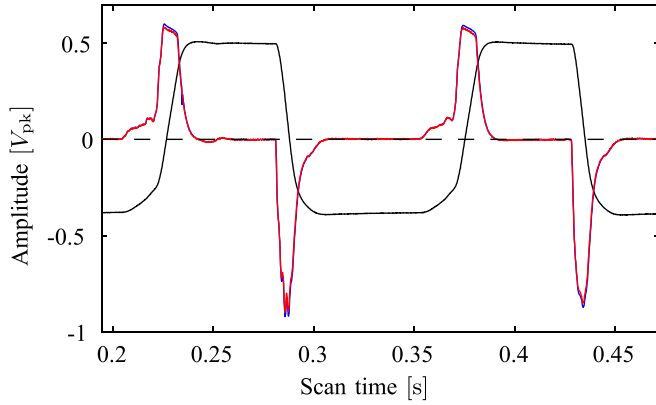


Fig. 6. Scaled estimated topography (—) of a TGZ3 calibration grating and the demodulated amplitude signal (error signal) with the LIA (—) and Kalman filter (—).

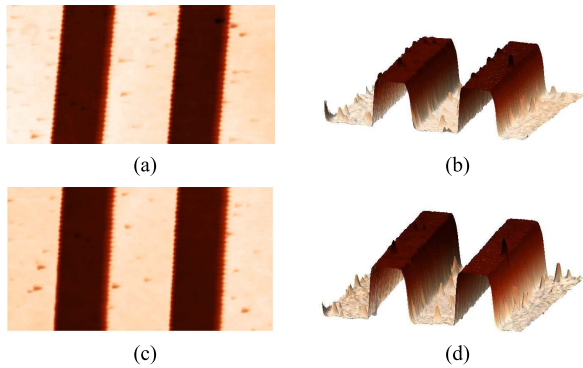


Fig. 7. 2-D and 3-D images obtained from the scan of a TGZ1 grating at $20 \mu\text{m/s}$ with (a) and (b) LIA and (c) and (d) Kalman filter in closed loop.

that the external LIA and Kalman filter yield almost identical amplitude estimates and no performance degradation can be observed. Since the scan speed is low, the low-pass filter of the external demodulator could be set to 3 kHz.

As the NT-MDT AFM does not allow for external demodulators to be used in the z -axis feedback loop, the existing system was altered to allow the Kalman filter to be

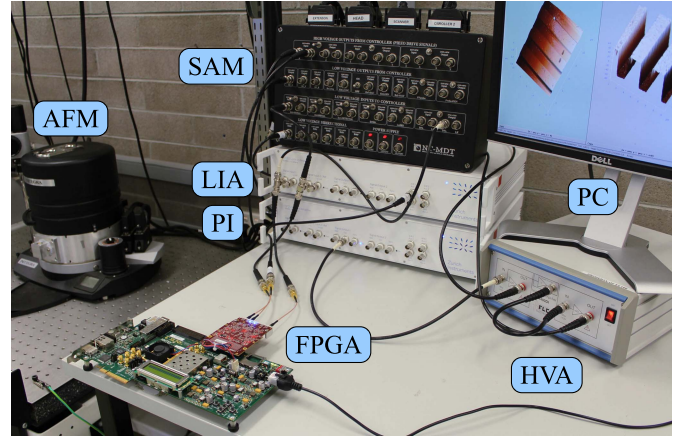


Fig. 8. Experimental setup to demonstrate the Kalman filter implemented on the FPGA in closed loop. The signal access module of the AFM provides the cantilever deflection output, cantilever drive input, and high voltage z -axis piezotube input.

tested in closed loop. The internal PI controller and electronics were bypassed with an external PI controller and high-voltage amplifier to drive the piezoelectric tube. The experimental setup is shown in Fig. 8. Two Zürich Instruments HF2LI were used, one as a reference LIA and the other one as the external PI controller. With this setup, images of an NT-MDT TGZ1 calibration grating with periodic features of height $h = 21.6 \pm 1.5$ nm were obtained. Fig. 7 highlights that there is no loss of image quality when comparing the scans obtained with the external Zürich Instruments LIA with a low-pass filter of 3 kHz and the Kalman filter in closed loop.

VI. CONCLUSION

This contribution outlines the implementation of a Kalman filter for high-bandwidth amplitude estimation in dynamic mode AFM. In order to demonstrate the true high-bandwidth nature of the Kalman filter and its superiority with respect to the LIA, a high-speed TM-AFM system is necessary. One of the major difficulties with setting up such a system is related

to minimizing the time-delay associated with every component in the z -axis feedback loop, as shown in Fig. 4. In particular, assuming a fast nanopositioning stage and z -axis controller, the highly resonant cantilever is usually the bottleneck for high-speed tapping-mode operation; the response of the cantilever to sudden topographical changes can be approximated by $(\omega_0/2Q)$ [5], where ω_0 and Q are the cantilever resonance frequency and Q -factor, respectively. This limitation demands cantilevers with resonance frequencies in the megahertz range and/or lowering the Q -factor which can be obtained via Q -control [34], [35] or by performing the experiments in liquid. The authors believe that the proposed Kalman filter will find its way into high-speed AFM setups where the significance of the presence of multifrequency components in the cantilever deflection demands greater flexibility in the amplitude estimation technique.

ACKNOWLEDGMENT

The research was performed in the Laboratory for Dynamics and Control of Nanosystems at the University of Newcastle, Callaghan, NSW, Australia. The authors would like to thank Y. K. Yong for the support in acquiring the experimental results with the custom-built nanopositioner.

REFERENCES

- [1] G. Binnig, C. F. Quate, and C. Gerber, "Atomic force microscope," *Phys. Rev. Lett.*, vol. 56, pp. 930–933, Mar. 1986.
- [2] D. Sarid, *Scanning Force Microscopy With Applications to Electric, Magnetic and Atomic Forces*. London, U.K.: Oxford Univ. Press, 1994.
- [3] Q. Zhong, D. Inniss, K. Kjoller, and V. B. Elings, "Fractured polymer/silica fiber surface studied by tapping mode atomic force microscopy," *Surf. Sci.*, vol. 290, nos. 1–2, pp. L688–L692, 1993.
- [4] T. Ando, "High-speed atomic force microscopy coming of age," *Nanotechnology*, vol. 23, no. 6, p. 062001, 2012.
- [5] T. Ando, T. Uchihashi, and T. Fukuma, "High-speed atomic force microscopy for nano-visualization of dynamic biomolecular processes," *Prog. Surf. Sci.*, vol. 83, nos. 7–9, pp. 337–437, 2008.
- [6] T. Ando, N. Kodera, E. Takai, D. Maruyama, K. Saito, and A. Toda, "A high-speed atomic force microscope for studying biological macromolecules," *Proc. Nat. Acad. Sci. USA*, vol. 98, no. 22, pp. 12468–12472, 2001.
- [7] T. Uchihashi, T. Ando, and H. Yamashita, "Fast phase imaging in liquids using a rapid scan atomic force microscope," *Appl. Phys. Lett.*, vol. 89, no. 21, p. 213112, 2006.
- [8] J. Kokavecz, Z. Tóth, Z. L. Horváth, P. Heszler, and Á. Mechler, "Novel amplitude and frequency demodulation algorithm for a virtual dynamic atomic force microscope," *Nanotechnology*, vol. 17, no. 7, p. S173, 2006.
- [9] D. Y. Abramovitch, "Low latency demodulation for atomic force microscopes, part I: Efficient real-time integration," in *Proc. Amer. Control Conf.*, Jun./Jul. 2011, pp. 2252–2257.
- [10] D. Y. Abramovitch, "Low latency demodulation for atomic force microscopes, part II: Efficient calculation of magnitude and phase," in *Proc. IFAC 18th World Congr.*, 2011, pp. 12721–12726.
- [11] R. García and E. T. Herruzo, "The emergence of multifrequency force microscopy," *Nature Nanotechnol.*, vol. 7, pp. 217–226, Apr. 2012.
- [12] K. S. Karvinen and S. O. R. Moheimani, "A high-bandwidth amplitude estimation technique for dynamic mode atomic force microscopy," *Rev. Sci. Instrum.*, vol. 85, no. 2, p. 023707, 2014.
- [13] A. Sebastian, M. V. Salapaka, D. J. Chen, and J. P. Cleveland, "Harmonic analysis based modeling of tapping-mode AFM," in *Proc. Amer. Control Conf.*, vol. 1, 1999, pp. 232–236.
- [14] A. Sebastian, M. V. Salapaka, D. J. Chen, and J. P. Cleveland, "Harmonic and power balance tools for tapping-mode atomic force microscope," *J. Appl. Phys.*, vol. 89, no. 11, pp. 6473–6480, 2001.
- [15] D. R. Sahoo, A. Sebastian, and M. V. Salapaka, "Transient-signal-based sample-detection in atomic force microscopy," *Appl. Phys. Lett.*, vol. 83, no. 26, pp. 5521–5523, 2003.
- [16] A. Sebastian, D. R. Sahoo, and M. V. Salapaka, "An observer based sample detection scheme for atomic force microscopy," in *Proc. 42nd IEEE Conf. Decision Control*, vol. 3, Dec. 2003, pp. 2132–2137.
- [17] D. R. Sahoo, P. Agarwal, and M. V. Salapaka, "Transient force atomic force microscopy: A new nano-interrogation method," in *Proc. Amer. Control Conf.*, Jul. 2007, pp. 2135–2140.
- [18] D. R. Sahoo, A. Sebastian, and M. V. Salapaka, "Harnessing the transient signals in atomic force microscopy," *Int. J. Robust Nonlinear Control*, vol. 15, no. 16, pp. 805–820, 2005.
- [19] K. S. Karvinen, M. G. Ruppert, K. Mahata, and S. O. R. Moheimani, "Direct tip-sample force estimation for high-speed dynamic mode atomic force microscopy," *IEEE Trans. Nanotechnol.*, vol. 13, no. 6, pp. 1257–1265, Nov. 2014.
- [20] C. Kitchin and L. Counts, *RMS to DC Conversion Application Guide*. Norwood, MA, USA: Analog Devices, Inc., 1986.
- [21] N. Kodera, D. Yamamoto, R. Ishikawa, and T. Ando, "Video imaging of walking myosin V by high-speed atomic force microscopy," *Nature*, vol. 468, no. 7320, pp. 72–76, 2010.
- [22] *HF2 User Manual*, Zürich Instruments, Revision 26211, Zürich, Switzerland, 2014.
- [23] B. Razavi, "Architectures and circuits for RF CMOS receivers," in *Proc. IEEE Custom Integr. Circuits Conf.*, May 1998, pp. 393–400.
- [24] K. S. Karvinen and S. O. R. Moheimani, "Modulated-demodulated control: Q control of an AFM microcantilever," *Mechatronics*, vol. 24, no. 6, pp. 661–671, 2014.
- [25] A. K. Cline, C. B. Moler, G. W. Stewart, and J. H. Wilkinson, "An estimate for the condition number of a matrix," *SIAM J. Numer. Anal.*, vol. 16, no. 2, pp. 368–375, 1979.
- [26] A. A. Girgis and T. L. D. Hwang, "Optimal estimation of voltage phasors and frequency deviation using linear and non-linear Kalman filtering: Theory and limitations," *IEEE Trans. Power App. Syst.*, vol. PAS-103, no. 10, pp. 2943–2951, Oct. 1984.
- [27] R. G. Brown and P. Y. C. Hwang, *Introduction to Random Signals and Applied Kalman Filtering*. New York, NY, USA: Wiley, 1997.
- [28] D. Simon, *Optimal State Estimation: Kalman, H Infinity, and Nonlinear Approaches*. New York, NY, USA: Wiley, 2006.
- [29] R. W. Stark and W. M. Heckl, "Higher harmonics imaging in tapping-mode atomic-force microscopy," *Rev. Sci. Instrum.*, vol. 74, no. 12, pp. 5111–5114, 2003.
- [30] N. F. Martínez *et al.*, "Bimodal atomic force microscopy imaging of isolated antibodies in air and liquids," *Nanotechnology*, vol. 19, no. 38, p. 384011, 2008.
- [31] J. Mertz, O. Marti, and J. Mlynek, "Regulation of a microcantilever response by force feedback," *Appl. Phys. Lett.*, vol. 62, no. 19, pp. 2344–2346, 1993.
- [32] Y. K. Yong, B. Bhikkaji, and S. O. R. Moheimani, "Design, modeling, and FPAA-based control of a high-speed atomic force microscope nanopositioner," *IEEE/ASME Trans. Mechatronics*, vol. 18, no. 3, pp. 1060–1071, Jun. 2013.
- [33] Y. K. Yong and S. O. R. Moheimani, "Collocated Z-axis control of a high-speed nanopositioner for video-rate atomic force microscopy," *IEEE Trans. Nanotechnol.*, vol. 14, no. 2, pp. 338–345, Mar. 2015.
- [34] M. W. Fairbairn and S. O. R. Moheimani, "Resonant control of an atomic force microscope micro-cantilever for active Q control," *Rev. Sci. Instrum.*, vol. 83, no. 8, pp. 083708-1–083708-9, 2012.
- [35] M. G. Ruppert, M. W. Fairbairn, and S. O. R. Moheimani, "Multi-mode resonant control of a microcantilever for atomic force microscopy," in *Proc. IEEE/ASME Int. Conf. Adv. Intell. Mechatronics*, Wollongong, NSW, Australia, Jul. 2013, pp. 77–82.



Michael G. Ruppert (S'14) received the Dipl.-Ing. degree in automation technology in production with a specialization in systems theory and automatic control from the University of Stuttgart, Stuttgart, Germany, in 2013. He is currently pursuing the Ph.D. degree in electrical engineering from The University of Newcastle, Callaghan, NSW, Australia.

He holds post-graduate research scholarships with The University of Newcastle and CSIRO, Clayton, VIC, Australia. His current research interests include the utilization of system theoretic tools in multifrequency atomic force microscopy and multimode Q control of microcantilevers.

Mr. Ruppert received the Academic Merit Scholarship and the Baden-Württemberg Scholarship.



Kai S. Karvinen (M'15) received the B.E. (Hons.) degree in electrical engineering and the B.Sc. degree in applied physics from Curtin University, Bentley, WA, Australia, in 2009, and the Ph.D. degree in electrical engineering from The University of Newcastle, Callaghan, NSW, Australia, in 2014.

His current research interests include the implementation and development of control and estimation techniques for high-bandwidth dynamic mode atomic force microscopy and quantum optics.

Dr. Karvinen received the Digby Leach Medal, the Engineers Australia Electrical College Bruce James Medal, and the Physics Graduate Award for his outstanding academic achievements.



Samuel L. Wiggins received the B.E. degree in mechatronics from The University of Newcastle, Callaghan, NSW, Australia, in 2014.

He was involved in his program with an emphasis on control theory, estimation methods, and embedded system with honors class 2. He is currently with the pharmaceutical industry.



S. O. Reza Moheimani (F'11) currently holds the James von Ehr Distinguished Chair in Science and Technology with the Department of Mechanical Engineering, University of Texas at Dallas, Dallas, TX, USA. His current research interests include ultrahigh-precision mechatronic systems, with a particular emphasis on dynamics and control at the nanometer scale, including applications of control and estimation in nanopositioning systems for high-speed scanning probe microscopy and nanomanufacturing, modeling and control of microcantilever-based devices, control of microactuators in microelectromechanical systems, and design, modeling, and control of micromachined nanopositioners for on-chip scanning probe microscopy.

Dr. Moheimani is a fellow of the International Federation of Automatic Control (IFAC) and the Institute of Physics, U.K. His research was recognized with a number of awards, including the IFAC Nathaniel B. Nichols Medal in 2014, the IFAC Mechatronic Systems Award in 2013, the IEEE Control Systems Technology Award in 2009, the IEEE TRANSACTIONS ON CONTROL SYSTEMS TECHNOLOGY Outstanding Paper Award in 2007, and several best student paper awards in various conferences. He has served on the Editorial Boards of a number of journals, including the IEEE TRANSACTIONS ON MECHATRONICS, the IEEE TRANSACTIONS ON CONTROL SYSTEMS TECHNOLOGY, and *Control Engineering Practice*. He is also the Chair of the IFAC Technical Committee on Mechatronic Systems, and has been the Chair of several international conferences and workshops.